Medical Image Analysis 35 (2017) 599–609

Contents lists available at ScienceDirect

Medical Image Analysis

journal homepage: www.elsevier.com/locate/media

Towards patient-specific modeling of mitral valve repair: 3D transesophageal echocardiography-derived parameter estimation

Fan Zhang[a,*], Jingjing Kanik[a], Tommaso Mansi[d], Ingmar Voigt[d], Puneet Sharma[d], Razvan Ioan Ionasec[d], Lakshman Subrahmanyan[e], Ben A. Lin[e], Lissa Sugeng[e], David Yuh[f], Dorin Comaniciu[d], James Duncan[a,b,c]

[a] Department of Biomedical Engineering, Yale University, New Haven, USA
[b] Department of Electrical Engineering, Yale University, New Haven, USA
[c] Department of Diagnostic Radiology and Biomedical Imaging, Yale University, New Haven, USA
[d] Siemens Corporation, Corporate Technology, Imaging and Computer Vision, Princeton, USA
[e] Section of Cardiovascular Medicine, Yale School of Medicine, New Haven, USA
[f] Section of Cardiac Surgery, Yale School of Medicine, New Haven, USA

ARTICLE INFO

Article history:
Received 15 April 2015
Revised 12 September 2016
Accepted 19 September 2016
Available online 27 September 2016

Keywords:
Mitral valve
Patient-specific model
Transesophageal echocardiography
Finite element biomechanical model
Mitral valve closure simulation

ABSTRACT

Transesophageal echocardiography (TEE) is routinely used to provide important qualitative and quantitative information regarding mitral regurgitation. Contemporary planning of surgical mitral valve repair, however, still relies heavily upon subjective predictions based on experience and intuition. While patient-specific mitral valve modeling holds promise, its effectiveness is limited by assumptions that must be made about constitutive material properties. In this paper, we propose and develop a semi-automated framework that combines machine learning image analysis with geometrical and biomechanical models to build a patient-specific mitral valve representation that incorporates image-derived material properties. We use our computational framework, along with 3D TEE images of the open and closed mitral valve, to estimate values for chordae rest lengths and leaflet material properties. These parameters are initialized using generic values and optimized to match the visualized deformation of mitral valve geometry between the open and closed states. Optimization is achieved by minimizing the summed Euclidean distances between the estimated and image-derived closed mitral valve geometry. The spatially varying material parameters of the mitral leaflets are estimated using an extended Kalman filter to take advantage of the temporal information available from TEE. This semi-automated and patient-specific modeling framework was tested on 15 TEE image acquisitions from 14 patients. Simulated mitral valve closures yielded average errors (measured by point-to-point Euclidean distances) of 1.86 ± 1.24 mm. The estimated material parameters suggest that the anterior leaflet is stiffer than the posterior leaflet and that these properties vary between individuals, consistent with experimental observations described in the literature.

1. Introduction

1.1. Motivation

The mitral valve apparatus is a complex anatomical unit composed of the mitral annulus, anterior and posterior valve leaflets, and chordae tendineae that tether the leaflets to papillary muscles (as shown in Fig. 1). While problems with either opening or closing can cause symptoms, mitral regurgitation is much more prevalent than mitral stenosis, especially in developed countries (Mann et al., 2014). Mitral regurgitation can be classified as either primary (with anatomic valvular pathology) or secondary (with functional abnormality despite normal valve leaflets). The preferred intervention for severe primary mitral regurgitation is valvular repair, when possible, rather than replacement. Surgical mitral valve repair, however, is a technically challenging operation that requires considerable expertise to achieve optimal outcomes (Nishimura et al., 2016). The procedure typically involves leaflet resection and annuloplasty ring placement. Occasionally, there may be placement of edge-to-edge leaflet sutures or artificial chords (Glower, 2012).

Noninvasive imaging of the mitral valve by transesophageal echocardiography (TEE) is critical to treatment planning. TEE, espe-

* Corresponding author.
E-mail address: fan.zhang@yale.edu (F. Zhang).

http://dx.doi.org/10.1016/j.media.2016.09.006
1361-8415/

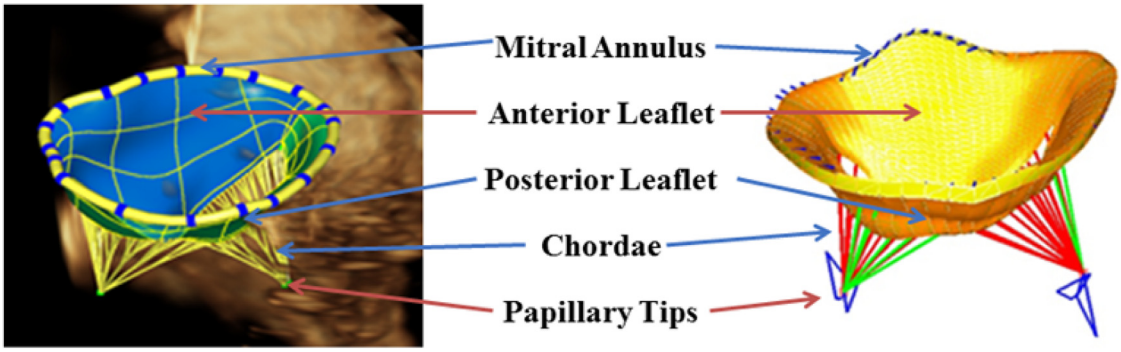

Fig. 1. Mitral valve apparatus represented by triangular meshes (left) and tetrahedron finite element meshes (right). The blue trajectories of the papillary tips on the right indicate the estimated motion of papillary tip from TEE images.

cially with three-dimensional imaging, allows definitive classification of the mechanism of mitral regurgitation and allows surgeons to estimate the likelihood of a successful repair. While patient-specific anatomic and functional information can be visualized with this approach, the prediction of outcomes is still primarily based upon the surgeon's experience and intuition.

There has been growing interest in developing tools to allow patient-specific modeling, both static and dynamic, of mitral valve anatomy and function (Sun et al., 2014; Kunzelman et al., 2007). These models can generally be categorized as either geometrical or biomechanical models. Geometrical models use semi-automated or automated analysis of medical images to reconstruct the mitral valve apparatus, track the motion of its components, and provide quantitative measurements. While these parameters can be used to evaluate mitral valve geometry and dynamics, they have limited ability to predict behavior after pathologic changes or interventions. Biomechanical models attempt to simulate mitral valve dynamics by incorporating initial geometry, assumed constitutive properties, and boundary conditions. Direct predictions can then be made regarding postsurgical function.

While increasingly sophisticated biomechanical models have been developed, truly patient-specific mitral valve modeling has not been fully realized yet. An important limitation involves the inability to accurately estimate in vivo tissue properties. Typical investigations of mitral valve material properties have been performed on in vitro specimens from animals or humans whose characteristics may or may not be similar to those of specific patients. Such studies have, in fact, shown that aging, hypertension, and myxomatous degeneration are all associated with altered mechanical properties (Pham and Sun, 2014; Stephens et al., 2009; Barber et al., 2001). It seems likely that the degree of myxomatous degeneration (the most common cause of primary mitral regurgitation) will also have an effect. A different approach is to obtain invasive in vivo measurements in animals (e.g., from sonomicrometers sutured to the leaflets (Rausch et al., 2013)), but these values will also have limited applicability to specific patients. Accordingly, development of methods to estimate in vivo patient-specific tissue properties through noninvasive imaging would be extremely helpful towards allowing mitral valve modeling to become useful in clinical practice (Sun et al., 2014).

The study presented here uses an approach combining image analysis and biomechanics in order to perform patient-specific mitral valve modeling. Three-dimensional TEE images are used in a semi-automated personalization framework that estimates chordae rest lengths and leaflet material parameters. In other words, the biomechanical model is iteratively calibrated to image-based observations to find an optimized set of geometric and biomechanical parameters describing the mitral valve dynamics for the patient whose echocardiographic images are being analyzed.

1.2. Aims of the study: patient-specific modeling of mitral valve

The goal of the study is to develop streamlined framework to build patient-specific biomechanical models based on information from medical images. The study presented in this paper extends our previous work (Kanik et al., 2013a; 2013b) from three perspectives: First, a comprehensive framework is described to personalize biomechanical models based on medical images. This framework is not limited to a specific biomechanical model or image modality. Second, the chordae optimization algorithm is improved with better computational efficiency. Third, the framework is tested on a larger data set of 15 clinical examples. The rest of the paper is organized as follows. The framework for patient-specific model is presented in Section 2 including the image analysis module, biomechanical model module and optimization module. The framework is evaluated on 15 examples to simulate mitral valve closure and the simulation results are compared to the ground truth in Section 3. Finally, the paper is concluded with discussions in Sections 4 and 5.

2. Methods

An overview of the framework is shown in Fig. 2. It starts from 3D real time TEE images and applies an image processing algorithms to estimate the geometry and dynamics of the mitral valve (Section 2.1). The image analysis module outputs finite element meshes of the mitral valve at open state ($\mathbf{g}_0$) and closed state ($\mathbf{g}_N$). The open valve mesh $\mathbf{g}_0$ is fed into the biomechanical model to generate a simulated closed valve geometry $\hat{\mathbf{g}}_N$ (Section 2.2). $\hat{\mathbf{g}}_N$ is then compared to the segmented $\mathbf{g}_N$ to adjust the interested biomechanical parameter set $\mathbf{p}$, which consists of chordae rest length set $\mathbf{l}$ and material property set $\mathbf{m}$. $\mathbf{l}$ and $\mathbf{m}$ are optimized separately in two steps: $\mathbf{l}$ is first optimized based on the simulated valve morphology (Section 2.3.2), and $\mathbf{m}$ is optimized using an extended kalman filter (EKF) framework (Section 2.3.3). After iterations, the algorithm outputs an estimated parameter $\hat{\mathbf{p}}$ when $\hat{\mathbf{g}}_N$ is close enough to $\mathbf{g}_N$. We review each of the modules in the following sub-sections.

2.1. Image analysis module

Various algorithms on mitral valve apparatus delineation and tracking have been proposed by different groups (Veronesi et al., 2009; Schievano et al., 2007; Burlina et al., 2010; Schneider et al., 2012; Zhou et al., 2012). The method of choice in this paper is a machine learning based algorithm proposed by Ionasec (2010). Compared to other works, it has several advantages: i) It is a comprehensive and anatomically driven model with well-defined and distinguishable anatomical landmarks. The landmark position

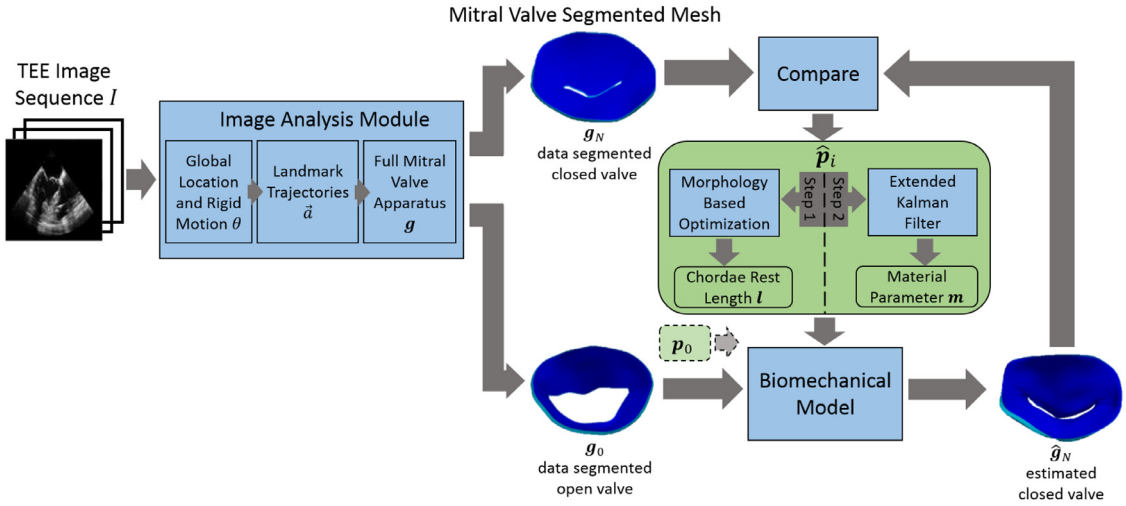

Fig. 2. Overview of the framework to build patient-specific model. $\mathbf{p}_0$ is an initialization of the parameter for the biomechanical model. The final output $\hat{\mathbf{p}} = [\hat{\mathbf{l}}, \hat{\mathbf{m}}]$ represents the personalized parameters for each patient.

can be adjusted by an expert to ensure accurate and reliable results. The average computational time for auto-detection is around 1 min, while the time for manual adjustment will vary, depending on the performance of the previous step and frame number. ii) The model provides inter- and intra- patient point correspondence through motion tracking. The point correspondence streamlines further comparison and evaluation. iii) The model was tested on 1516 TEE volumes with results demonstrating accuracy of 1.45 mm with respect to expert defined ground-truth.

In this module, the mitral valve structure (either open or closed) is segmented in three steps: i) global location and rigid motion estimation, ii) non-rigid landmark motion localization and estimation, iii) the comprehensive valve deformation estimation.

i) *Global location and rigid motion estimation*: The rigid valve motion at time t is parameterized as $\theta(t) = \{(c_x, c_y, c_z), (\vec{\alpha_x}, \vec{\alpha_y}, \vec{\alpha_z}), (s_x, s_y, s_z), t\}$, where (c_x, c_y, c_z), $(\vec{\alpha_x}, \vec{\alpha_y}, \vec{\alpha_z})$, (s_x, s_y, s_z) are the position, orientation and scale parameters, which define a bounding box around the valve. The problem is expressed as

$$\underset{\theta}{argmax}\, p(\theta \mid I) = \underset{\theta}{argmax}\, p(\theta(0), \cdots, \theta(n-1) \mid I(0), \cdots I(n-1)) \tag{1}$$

We utilize a marginal space learning (MSL) (Zheng et al., 2008) framework to re-formulate the probability at time t as

$$\begin{aligned} p(\theta(t) \mid I(t)) = {} & p(c_x, c_y, c_z \mid I(t)) \\ & p(\vec{\alpha_x}, \vec{\alpha_y}, \vec{\alpha_z} \mid c_x, c_y, c_z, I(t)) \\ & p(s_x, s_y, s_z \mid \vec{\alpha_x}, \vec{\alpha_y}, \vec{\alpha_z}, c_x, c_y, c_z, I(t)) \end{aligned} \tag{2}$$

which is maximized by using trained detectors at each marginal space. Random sample consensus (RANSEC)(Fischler and Bolles, 1981) estimators are employed to obtain a temporal consistent θ after estimating parameter candidates $\theta(t)$ at each time step t.ii) *Non-rigid landmark motion estimation*: 9 anatomical landmarks are defined including: a) 7 for the mitral leaflets: left and right trigone, the posteroannular midpoint, anterior and posterior commissures, anterior and posterior tip, and b) 2 for papillary muscle: anterior and posterior papillary tips. The objective is to find each landmark j and its trajectory $\vec{a^j}$ given I and θ

$$\underset{\vec{a^j}}{argmax}\, p\left(\vec{a^j} \mid I, \theta\right) \tag{3}$$

The problem can be more efficiently solved in discrete Fourier transform (DFT) spectrum space as

$$\underset{\vec{s^j}}{argmax}\, p\left(\vec{s^j} \mid I, \theta\right) \tag{4}$$

where $\vec{s^j}$'s are DFT coefficients of $\vec{a^j}$'s. The spectrum space is marginalized using the same MSL framework. The probability is maximized by applying detectors for each subspace that are trained with local-spatio-temporal features.iii) *Comprehensive valve deformation estimation*: The full mitral valve apparatus geometry $\mathbf{g}$ is represented using triangular meshes expanded from landmark trajectories $\vec{a^j}$'s. The surfaces in end-diastolic (ED) and end-systolic (ES) are first constructed using thin plate spline and refined by boundary detector and principle component analysis. The detectors are trained using a probabilistic boosting tree (PBT)(Tu, 2005) on multiscale steerable features (Yang et al., 2008). Non-rigid deformation is then propagated to the remaining frames using a learned prior. The valve geometry $\mathbf{g}$ of the whole sequence is refined by incorporating information from optical flow tracking and boundary detection tracker.

For more details about the image analysis module, we recommend readers refer to the paper from Ionasec (2010).

2.2. Biomechanical module

The open valve geometry mesh generated from the previous image analysis module is fed into the biomechanical module to simulate the closed valve geometry. There is a variety of valve biomechanical models available developed by different groups (Hammer et al., 2012; Wang and Sun, 2013; Stevanella et al., 2011; Votta et al., 2013; Sprouse et al., 2013; Einstein et al., 2010; Watton et al., 2008). In this paper we adopt a finite element model proposed by Mansi et al. (2012) for the following reasons: i) The model is well integrated with patient-specific anatomies and boundary conditions. ii) The model simulates the mitral valve closure in an automatic and fast manner (average 12 min per simulation). The automation helps streamline the process. The fast computing power takes the patient-specific model one step closer into the application of therapy planning. iii) The model demonstrates reasonable overall prediction power. The valve closure simulation has been tested on 25 cases. A case of mitral valve repair prediction is presented in Mansi's paper, which describes a comparison of the simulated valve function to the clinical observation (Fig. 3).

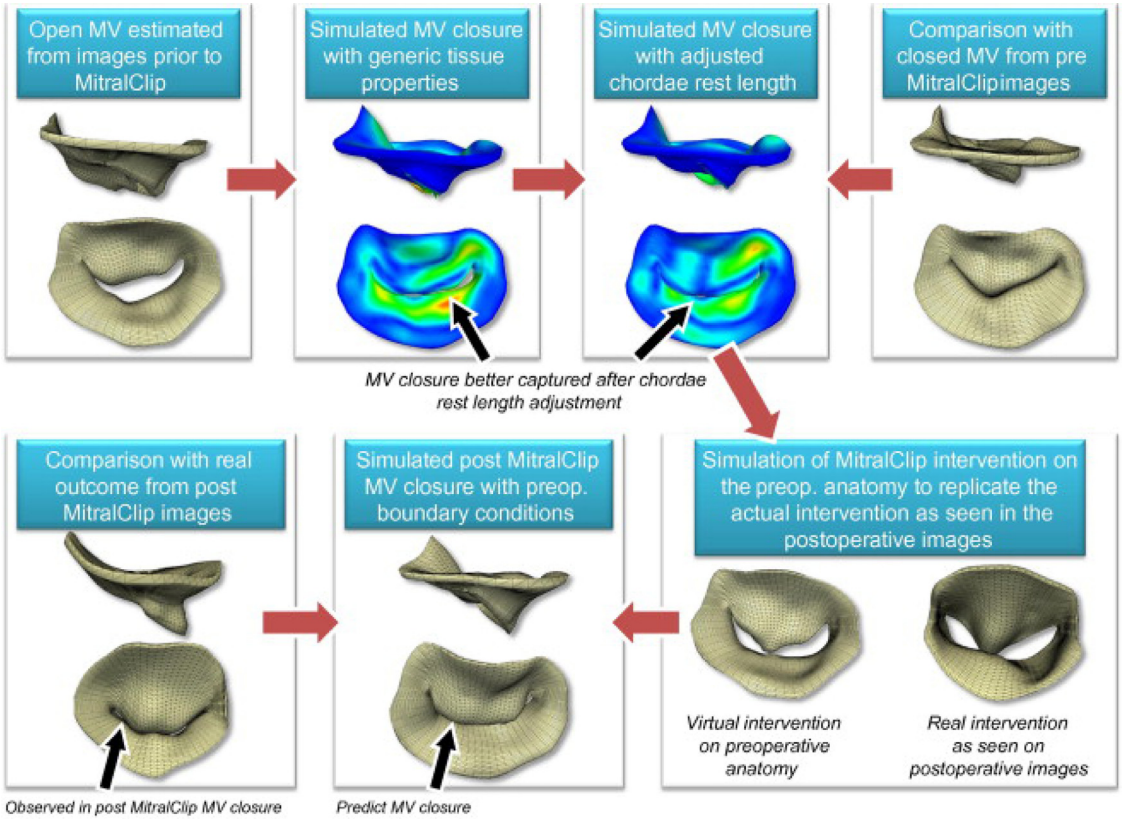

Fig. 3. Simulated MitralClip intervention on the preoperative anatomy of one patient and comparing the result with the real outcome. (Mansi et al., 2012; use by permission)

iv) The model is also fully capable of handling the finite deformation range of values inherent to this problem.

In this model, the leaflets are discretized into tetrahedron finite elements. 28 marginal chordae are attached between papillary tip and leaflet edges and 8 basal chordae are attached between papillary tips and leaflet belly. The insertion points of the chordae are identical for all patients leveraging the point correspondence of the model. The mitral leaflets are assumed to be composed of collagen fibers which are mainly parallel to the annulus in the circumferential direction with those close to the commissures gradually rotating to be perpendicular to the annulus in the radial direction for the anterior leaflet. The fiber direction is modeled in the same way as Prot et al. did (Prot et al., 2009; Prot and Skallerud, 2009) which has also been reported in experimental observations (May-Newman and Yin, 1995).

Mitral leaflets are modeled as linear, transversely isotropic and nearly incompressible materials since it is considered to be close approximation in a few biomechanical models (Hammer et al., 2008; Krishnamurthy et al., 2009; Schievano et al., 2009; Votta et al., 2013). Some recent in-vivo animal studies suggest that the mitral valve tends to exhibit linear behavior in the physiological range (Krishnamurthy et al., 2008; 2009). A study from Comas et al. suggests that co-rotational FEM is able to capture tissue deformation (Comas et al., 2008). Despite the linear discretization of the Lagrangian strain, the co-rotational framework controls the artificial dilation during rotation. Five elastic parameters are needed to describe such materials. In order to represent the leaflet incompressibility and also to ensure system stability, Poisson's ratio for both the symmetry plane and its normal direction are set to 0.488 (Mansi et al., 2012). The remaining three elastic parameters include Young's modulus in the fiber direction, Young's modulus and shear modulus in the cross fiber direction, denoted as E_f, $E_{f\perp}$ and $G_{f\perp}$ respectively in this paper. The Young's modulus corresponding to the tangent elastic modulus measured at large strains by Schievano et al. (2009) are used as shown in Table 1. The chordae are modeled as piece-wise tensile springs and Young's modulus at different strain estimated experimentally by Kunzelman and Cochran (1990) are used as shown in Table 1.

Table 1
Elastic parameters of mitral leaflets and chordae. A_0 is the area of cross section of the chordae and ε is the chordae strain.

Leaflets (Schievano et al., 2009)	
Anterior leaflet Young's modulus	$E_f = 6.233MPa, E_{f\perp} = 2.350MPa$
Anterior leaflet Shear modulus	$G_{f\perp} = 1.369MPa$
Posterior leaflet Young's modulus	$E_f = 2.087MPa, E_{f\perp} = 1.887MPa$
Posterior leaflet Shear modulus	$G_{f\perp} = 0.694MPa$
Marginal Chordae (Kunzelman and Cochran, 1990)	
Young's modulus	$E = \begin{cases} 312g/mm^2, \varepsilon < 2.5\% \\ 3406g/mm^2, \varepsilon \geq 2.5\% \end{cases}$
Cross section	$A_0 = 0.40mm^2$
Basal Chordae (Kunzelman and Cochran, 1990)	
Young's modulus	$E = \begin{cases} 66g/mm^2, \varepsilon < 2.5\% \\ 2120g/mm^2, \varepsilon \geq 2.5\% \end{cases}$
Cross section	$A_0 = 2.05mm^2$

The mitral valve closure is simulated by solving the system dynamics equation:

$$M\ddot{U} + C\dot{U} + KU = F_c + F_p \tag{5}$$

where U is the displacement vector of the vertices of the mitral valve mesh. $\dot{U}$ and $\ddot{U}$ are the velocity and acceleration respectively. M is the diagonal mass matrix (a uniform mass density $\rho = 1.04$ g/ml is used). K is the stiffness matrix and a function of material parameters. C is the Raleigh damping matrix ($C = \alpha_M M + \alpha_K K, \alpha_M = 0.1s^{-1}, \alpha_K = 0.1s$) which models the viscosity of the system and controls the stability of the system. F_c and F_p are the forces developed by the chordae and heart pressure respec-

tively. The heart pressure is modeled by a generic pressure profile that increases from 0 mmHg to 120 mmHg. The force induced by each chordae f_c is related to the chordae rest length and F_c is the sum of all f_c. The motions of the papillary tips and the mitral annulus estimated from TEE images are prescribed as boundary conditions.

For geometry $\hat{\mathbf{g}}_i$ at time i, after displacement vector U_i at that time frame is solved, the valve geometry in the next frame is estimated by

$$\hat{\mathbf{g}}_{i+1} = \hat{\mathbf{g}}_i + U_i \tag{6}$$

where U_i is a function of a series of biomechanical parameters $\mathbf{p}$. Overall, the close valve geometry $\hat{\mathbf{g}}_N$ can be represented as a function of $\mathbf{g}_0$ and $\mathbf{p}$, $\hat{\mathbf{g}}_N = h(\mathbf{g}_0, \mathbf{p})$, where h is the biomechanical module.

2.3. Optimization algorithm

2.3.1. Overview

The set of parameters that requires personalization is denoted as $\mathbf{p} = [\mathbf{l}, \mathbf{m}]$, where $\mathbf{l}$ is the vector of chordae rest length and $\mathbf{m}$ is vector of the material parameters. There are 28 marginal chordae attached to the edge of the leaflets and 8 basal chordae attached to the belly of the leaflets, so there are 36 parameters in the vector $\mathbf{l}$, $\mathbf{l} = [l_1, l_2, \ldots l_{36}]$. The leaflet tissues are approximated as transversely isotropic elastic material so three free material parameters are used to describe the tissue property for each element including Young's modulus along the fiber E_f, Young's modulus across the fiber $E_{f\perp}$ and shear modulus G. Poisson's ratio are fixed as $\nu = 0.488$ since the leaflet tissue are assumed to be nearly incompressible. The number of parameters in vector $\mathbf{m}$ ($\mathbf{m} = \left[m^1, m^2, \ldots, m^N\right]$) is dependent on the number of the regions where material parameters vary and the inter-dependent relationship of the three specific material parameters (E_f, $E_{f\perp}$ and G). We start from a simple assumption and a strong constraint on the parameters to ensure the estimation results can be interpreted with physiological meaning. It is assumed that material parameters are different for the anterior and posterior leaflet, but are homogeneous on each respective leaflet. In addition, the ratio of the Young modulus along and across the fiber ($r = E_f/E_{f\perp}$) is fixed and the shear modulus is approximated by $G \approx E_f/(2((1+\nu)))$. Under those assumptions and constraints, two material parameters are estimated $\left(m = \left[m^1, m^2\right] = \left[E_f^{Anterior}, E_f^{Posterior}\right]\right)$ and another four parameters ($E_{f\perp}^{Anterior}$, $E_{f\perp}^{Posterior}$, $G^{Anterior}$, $G^{Posterior}$) are derived from these two. The set of parameters to be personalized can be written as

$$\mathbf{p} = \left[l_1, l_2, \ldots l_{36}, m^1, m^2\right] \tag{7}$$

The goal of personalizing the parameters is to simulate the mitral valve closure as closely as possible to image based observations. The personalization problem can be formulated as an optimization procedure where the objective function is the sum of the differences of the Euclidean point-to-point distances of the biomechanical model derived and image estimated mitral valve closure. The objective function is minimized with respect to $\mathbf{p}$ to estimate the patient-specific parameters as follows:

$$\hat{\mathbf{p}} = \arg\min_{\mathbf{p}} f(\mathbf{p}) = \arg\min_{\mathbf{p}} \|\mathbf{g}_n - h(\mathbf{g}_0, \mathbf{p})\| \tag{8}$$

where $\mathbf{g}_0$ and $\mathbf{g}_n$ is the geometry of the mitral leaflets represented by the location of the vertices at the open and closed state, $h(\cdot)$ is the observation function derived from the biomechanical model loading (related to the chordae rest length in $\mathbf{p}$), the geometry at the open state (g_0), tissue property (related to the material parameters in $\mathbf{p}$), boundary condition, and dynamic equilibrium function (Eq. (5)).

A two-step optimization algorithm is developed to solve the optimization problem. It is shown in the sensitivity analysis that chordae rest length has greater influence quantitatively on simulation results than the material parameters. Therefore, chordae rest length is optimized in the first step to reduce the cost function as much as possible. Material parameters are then estimated in the second step given a reasonable simulation with personalized chordae rest length using the Extended Kalman Filter (EKF). Such two-step procedure mimics the coarse-to-fine framework to improve the optimization efficiency. The details of each step are described in Section 2.3.2 and 2.3.3.

2.3.2. Chordae rest length optimization

There are 36 parameters in the chordae rest length so it is computationally expensive to use exhaustive search algorithms. Gradient-based algorithms are not optimal since the parameters are not independent thus first order Taylor expansions are not sufficient to approximate the function and the gradient can only be calculated using finite different method. Powell's conjugate direction method (Powell, 1964) is not easily adoptable here since normal search vectors cannot be easily defined. Therefore we propose a morphology-guided search-based algorithm to optimize the chordae rest length in three steps.

First, the optimal starting values are searched from a set of values as shown in Table 2. Note that contrary to our intuitive understanding, measured Euclidean distance from papillary tip to chordae insertion points (both open and closed) may not always be a good initialization since the chordae may be folded or extended. The chordae rest length resulting in the smallest cost function is set to be the initial value.

Second, the chordae are adjusted by four groups according to their morphology: those attached to the i) anterior leaflet and anterior papillary tip, ii) the anterior leaflet and posterior papillary tip, iii) the posterior leaflet and posterior papillary tip, iv) the posterior leaflet and anterior papillary tip. Previous work (Kanik et al., 2013a) shows that greatest reduction in cost function happens when the chordae rest lengths are adjusted by group. During this step, only chordae groups with large discrepancy between insertion points and ground truth are adjusted (e.g. $\geq$ 3 mm).

Finally, in the fine tuning step, the chordae rest length is adjusted in each basal chordae (rather than by groups as in the previous step). If the surface of the simulated closed leaflets is above the ground truth, basal chordae are shortened. If the surface is below the ground truth, basal chordae are lengthened.

2.3.3. Material parameter optimization

The chordae rest length optimization brings the simulation result closer to the ground truth. Extended Kalman Filter (EKF) (Einicke and White, 1999) is used to inversely identify the material parameters for the mitral leaflets and further personalize the biomechanical model. EKF provides a basic stable sequential least square solution and has been shown to be effective for material parameter estimation of the left ventricle by Liu and Shi (2007); 2009). EKF has also been used for cardiac biomechanics estimation, which exhibits non-linear behavior (Marchesseau et al., 2015; Wong et al., 2011).

The mitral valve dynamics can be transformed into a state-space representation of a discrete-time nonlinear stochastic system including a process function and observation function. The process function $f(\cdot)$ states the assumption that material parameters stay constant during mitral valve closure ($\mathbf{m}_k = f(\mathbf{m}_{k-1}) = \mathbf{m}_{k-1}$). The observation function $h(\cdot)$ states that the biomechanical model derives mitral valve closure with the aim to match the observation from TEE images. The state-space representation is as follows:

$$\mathbf{m}_k = f(\mathbf{m}_{k-1}) + \mathbf{w}_{k-1} \tag{9}$$

Table 2
Chordae rest length optimization initial values.

	marginal chordae	basal chordae
1	25 mm	30 mm
2	25 mm	25 mm
3	30 mm	30 mm
4	Euclidean distance from papillary tip to chordae insertion point at end diastole	
5	Euclidean distance from papillary tip to chordae insertion point at early systole	

$$\mathbf{g}_k = h(\mathbf{m}_k) + \mathbf{v}_k \tag{10}$$

where k is the time point ($k = 1$ is the end diastole, $k = 2$ is the early systole under the current assumptions), $\mathbf{m}_k = [m_k^1, m_k^2]$ is the state vector namely the material parameters at the kth observation, $\mathbf{g}_k = [g_k^1, g_k^2, \ldots, g_k^{ele}] = [x_k^1, y_k^1, z_k^1, x_k^2, y_k^2, z_k^2, \ldots, x_k^{ele}, y_k^{ele}, z_k^{ele}]$ is the observation vector namely the vertices representing mitral leaflets (ele is the number of the vertices, $ele = 3248$ in the paper), $\mathbf{w}_{k-1}$ and $\mathbf{v}_k$ are the state and process noises respectively and assumed to follow Gaussian distributions with zero mean and covariance matrix Q_k and R_k.

The Extended Kalman Filter solves the optimization problem in three steps: i) The material parameters and the covariance matrix at $t = 1$ are initialized with prior knowledge of the state with mean $\hat{\mathbf{m}}_1$ and covariance matrix Σ of a Gaussian distribution. The mean is the generic material parameters derived from ex-vivo animal experiment and the same as Table 1. ii) Material parameters and its covariance matrix at the next time point are predicted based on process function (time update). iii) The prediction is corrected based on the observation function and measurements at the current time point (measurement update). The time update and measurement update continues until the last time point. The mathematical operation is described as follows:

Initialization:

$$\mathbf{m}_1 = \hat{\mathbf{m}}_1, P_1 = \Sigma \tag{11}$$

Prediction:

$$\begin{aligned} \mathbf{m}_k^f &\approx f\left(\mathbf{m}_{k-1}^a\right) = \mathbf{m}_{k-1}^a \\ \mathbf{P}_k^f &= \mathbf{J}_f\left(\mathbf{m}_{k-1}^a\right)\mathbf{P}_{k-1}\mathbf{J}_f^T\left(\mathbf{m}_{k-1}^a\right) + \mathbf{Q}_{k-1} \end{aligned} \tag{12}$$

Correction:

$$\begin{aligned} \mathbf{m}_k^a &\approx \mathbf{m}_k^f + \mathbf{K}_k(\mathbf{g}_k - h(\mathbf{m}_k)) \\ \mathbf{K}_k &= \mathbf{P}_k^f\mathbf{J}_h^T\left(\mathbf{m}_k^f\right)\left(\mathbf{J}_h\left(\mathbf{m}_k^f\right)\mathbf{P}_k^f\mathbf{J}_h^T\left(\mathbf{m}_k^f\right) + \mathbf{R}_k\right)^{-1} \\ \mathbf{P}_k &= \left(I - \mathbf{K}_k\mathbf{J}_h\left(\mathbf{m}_k^f\right)\right)\mathbf{P}_k^f \end{aligned} \tag{13}$$

where $\mathbf{J}_f$ and $\mathbf{J}_h$ are the Jacobian of $f(.)$ and $h(.)$, and $\mathbf{K}_k$ is the Kalman gain. The Jacobian of $h(.)$ is defined as

$$\mathbf{J}_h(\mathbf{m}) = \begin{bmatrix} \frac{\partial h_1}{\partial m_1} & \frac{\partial h_1}{\partial m_2} & \cdots & \frac{\partial h_1}{\partial m_j} \\ \vdots & & \ddots & \vdots \\ \frac{\partial h_n}{\partial m_1} & \frac{\partial h_n}{\partial m_2} & \cdots & \frac{\partial h_n}{\partial m_j} \end{bmatrix} \tag{14}$$

where $h(\mathbf{m}) = [h_1(\mathbf{m}), h_2(\mathbf{m}), \cdots, h_n(\mathbf{m})]$, $\mathbf{m} = \left[m_1, \cdots, m_J\right]$. The Jacobian of $f(.)$ is an identity matrix I under the assumption of constant material parameters through cardiac cycle. The Jacobian of $h(.)$ is calculated by the finite difference method as follows

$$\begin{aligned} \frac{\partial h(\mathbf{m})}{\partial m_j} &= \frac{h(\mathbf{m} + \triangle\mathbf{m}) - h(\mathbf{m})}{\triangle m_j} \\ \triangle\mathbf{m} &= \left[0, \cdots, \triangle m_j, \cdots, 0\right] \end{aligned} \tag{15}$$

An iterated EKF is used to solve this problem since there are only two time points involved in the estimation. The EKF iteration process is re-initialized with $\mathbf{m}_1 = \mathbf{m}_N, \mathbf{P}_1 = \mathbf{P}_N$ after each iteration until convergence or maximum iteration times.

3. Experiments and results

3.1. Data set and experiments

The performance of the personalization of the mitral valve biomechanical model is evaluated on 15 3D Real-Time TEE images from 14 patients. The images were randomly collected on patients diagnosed of various heart diseases including mitral valve diseases, aortic valve diseases, and myocardium infarction. The 3-D TEE acquisition used an iE33 Philips console with an X7-2t TEE probe with image resolution 0.75–1.58 mm. The average total number of frames is 16 and the mitral valve closure can be seen in two to five frames.

The dynamics of the mitral valve apparatus, including mitral annulus, anterior and posterior leaflets, and papillary tips, were first estimated by the image analysis algorithm described in Section 2.1. The results were then inspected by the users and modifications were made if necessary. A few criteria were used to ensure the accuracy of the image analysis results. First, the position of the key landmarks of the leaflets including the tips, commissures, trigones and the posteroannular midpoint were examined. Second, the area of anterior leaflet was larger than posterior leaflet for patients with normal mitral valve morphology. Third, the area of anterior and posterior leaflet did not change much from end diastole to early systole since the leaflet tissues are incompressible. Fourth, the location of the papillary tips were verified using both spatial and temporal information. Accurate image analysis results are essential for successful patient-specific biomechanical modeling since the image analysis results served as input for biomechanical model simulation and personalization.

3.2. Parameter estimation performance

3.2.1. Overview

In order to demonstrate how well the algorithm calibrates the biomechanical model for individual patients, the point-to-point Euclidean distances are calculated before and after the optimization on 15 examples for quantitative evaluation. As mentioned in Section 2.1, the point correspondence of the mitral leaflets at the open and closed configuration are established in the image analysis module. The mean and standard deviation of the Euclidean distances between all the corresponding points representing the mitral leaflets are presented in Table 3.

A two-sample t-test is performed to determine if the personalization algorithm has significantly improved the results of the simulation. The Euclidean distances before and after the personalization are the two sample data. The null hypothesis is that the errors represented by the distances before and after are with equal means and equal but unknown variances. The null hypothesis is rejected with p-value of 0.0012. The t-test proves that the personalization algorithm helps generate significantly different simulation results compared to before the algorithm is used. Since the distances are smaller after the personalization, the algorithm improves the simulation results by tuning related parameters. Among the 15 examples, 7 of them have average error reduced by more than 1 mm.

Table 3
The results of simulated mitral valve closure in the form of *mean* ± *std* in *mm* point-to-point Euclidean distances from the simulated mitral leaflet at the closed state and the ground truth. In the 'No optimization' column, marginal chordae rest length of 25 mm, basal chordae rest length of 30 mm and material parameters from Table 1 are used. In the 'Optimization I' column, chordae rest length are optimized for each patient and material parameters from Table 1 are used. In the 'Optimization II' column, optimized chordae rest length and material parameters are used.

Patient ID	No optimization	Optimization I	Optimization II
P1	3.17 ± 1.98	2.59 ± 1.59	2.52 ± 1.33
P2	2.92 ± 2.00	2.88 ± 2.12	2.55 ± 1.76
P3	2.23 ± 1.52	2.14 ± 1.44	2.03 ± 1.32
P4	1.78 ± 1.28	1.72 ± 1.20	1.72 ± 1.20
P5	3.39 ± 2.24	1.86 ± 1.21	1.83 ± 1.16
P6	1.77 ± 0.94	1.44 ± 0.93	1.41 ± 0.93
P7	2.79 ± 1.64	1.82 ± 1.20	1.82 ± 1.18
P8	6.42 ± 3.78	2.00 ± 1.27	1.92 ± 1.21
P9	2.87 ± 1.82	1.48 ± 1.04	1.48 ± 1.01
P10_1	4.53 ± 3.00	2.60 ± 1.75	2.50 ± 1.63
P10_2	3.34 ± 2.39	2.20 ± 1.63	2.12 ± 1.56
P11	2.30 ± 1.72	1.58 ± 1.07	1.58 ± 1.07
P12	1.83 ± 0.97	1.23 ± 0.75	1.16 ± 0.68
P13	2.99 ± 2.15	1.68 ± 1.16	1.62 ± 1.14
P14	5.73 ± 3.98	1.62 ± 1.35	1.61 ± 1.34

Using 25 mm and 30 mm as the marginal and basal chordae rest length and material parameters from Table 2, the average error for all examples is 3.20 ± 2.09 mm. The chordae rest length optimization reduced the error to 1.92 ± 1.31 mm (38.5%). The material parameter optimization reduces the average point-to-point distances from 1.92 ± 1.31 mm to 1.86 ± 1.24 mm (1.4%). The chordae rest length has a greater effect on the simulation results than the material parameters. The effect of both sets of parameters are analyzed independently in Sections 3.2.2 and 3.2.3.

3.2.2. Effect of chordae rest length optimization

Material parameters are fixed in Table 2 during chordae rest length optimization. Given the input of the mitral valve dynamics estimated from the TEE images, the algorithm builds the biomechanical model using 25 mm and 30 mm for the rest length of marginal and basal chordae respectively. The algorithm then optimizes the chordae rest length following three steps including searching for optimal starting value, morphology-guided group adjustment, and fine tuning on basal chordae. After the chordae rest length optimization, the output is the personalized chordae rest length and improved mitral valve closure from simulation.

The estimated average marginal and basal chordae rest length is 25.19 ± 3.56 mm and 27.16 ± 3.96 mm respectively. The average simulation error is reduced to 1.92 ± 1.31 mm which is comparable to the resolution of the TEE images (1 – 2 mm). The average number of iterations are 31 and the time each iteration takes depends on the number of frames from the open state to the closed state (Average number of frames is 3). Since the pressure loading is normalized, one frame takes about 3.33 min and one simulation takes about 10 min on average.

The biggest improvement of the simulation resulting from chordae rest length adjustment happens in the first step of setting the optimal starting value. The average simulation error are reduced from 3.20 ± 2.09 mm to 2.03 ± 1.33 mm. In the cases with large simulation error, the generic chordae rest length does not lead to successful simulation but the optimized starting value bring the average simulation error to 2 mm which is comparable to the image resolution. The qualitative effect of the chordae rest length is demonstrated using three examples. In each example, the ground truth, which is the mitral valve in open and closed configuration estimated from TEE images, is displayed in top and side view. The simulation error (Euclidean distances) at each vertices are displayed in the form of colored distance map.

3 examples are given (Fig. 4) to demonstrate the performance of chordae rest length optimization. In Fig. 4(i), the chordae rest length optimization brings the average simulation error from 3.17 ± 1.98 mm to 2.59 ± 1.59 mm. The mismatch is especially severe in the posterior leaflet (yellow and red region) before the optimization. The rest length adjustment brings the posterior on the left side up, the posterior on the right side down, and reduces the large distance area (red region) thus reducing the large regurgitation hole. In Fig. 4(ii), the chordae rest length optimization brings the average simulation error from 2.79 ± 1.64 mm to 1.82 ± 1.20 mm. The chordae rest length adjustment brings the mitral leaflet in the simulated mitral valve closure to a similar surface as the ground truth. The red and yellow region (indicating large distances) in both the anterior and posterior leaflet are mostly replaced by blue and green (indicating smaller distances). In Fig. 4(iii), the chordae rest length optimization brings the average Euclidean distances from 1.83 ± 0.97 mm to 1.23 ± 0.75 mm. The chordae rest length adjustment turns a large area of the yellow and green region into blue and closes the regurgitation hole slightly.

It is also worth noting that the results from image analysis constrains the capability of the biomechanical models. The details of the morphological features from the open state will be carried in the simulation results since leaflets are assumed to be incompressible tissue and the smooth deformation is used to avoid collision. In Fig. 4(i), the anterior leaflet is larger than in the open configuration than closed configuration and it is obvious from the side view. There is an 'extra' anterior leaflet in the simulated mitral valve closure which can only be fixed by more accurate image analysis results. In Fig. 4(ii), the only area with high errors (shown in red) is the bowl shape in the posterior leaflet is caused by a similar shape in the open configuration (from image analysis) where the mitral valve closure starts. In the Fig. 4(iii), the anterior and posterior leaflet may be nicely coapted if there were a little more anterior and posterior tissue at the regurgitation site from the open configuration.

3.2.3. Effect of material parameters optimization

After the chordae rest length optimization, the personalized chordae rest length is used in the biomechanical model during material parameter identification. The algorithm starts with a slightly different set of material parameters ($E_{f\perp}^{Anterior} = 2.351$ MPa, $E_{f\perp}^{Posterior} = 1.887$ MPa, $G^{Anterior} = 2.094$ MPa, $G^{Posterior} = 0.701$ MPa, covariance matrix $0.01I$) compared to the ones in Table 1 used during chordae rest length optimization because of the fixed relationship among the material parameters. The covariance matrix for the process and observation are set to be $Q_k = 0.01I$ and $R_k = 0.001I$ to allow for wider search space in the extended Kalman filter. The iterated process stops when the optimization converges or maximum number of iteration is reached.

The material parameter optimization reduces the average point-to-point distances from 1.92 ± 1.31 mm to 1.86 ± 1.24 mm (1.4%) which is much smaller compared to the chordae rest length optimization. The average number of iterations is 14 and each iteration takes about 10*min*. During each iteration, the most time-consuming parts include the biomechanical model simulation (three simulations running in parallel and each takes about 10 min) and the inversion of the matrix when calculating the Kalman gain (0.5 min). The estimated material parameters are shown in Table 4. It can be seen that the anterior leaflet is stiffer (with larger value of Young's modulus) than the posterior leaflet in all patients. Material parameters also vary among different patients. In the two examples from the same patient (P10_1 and

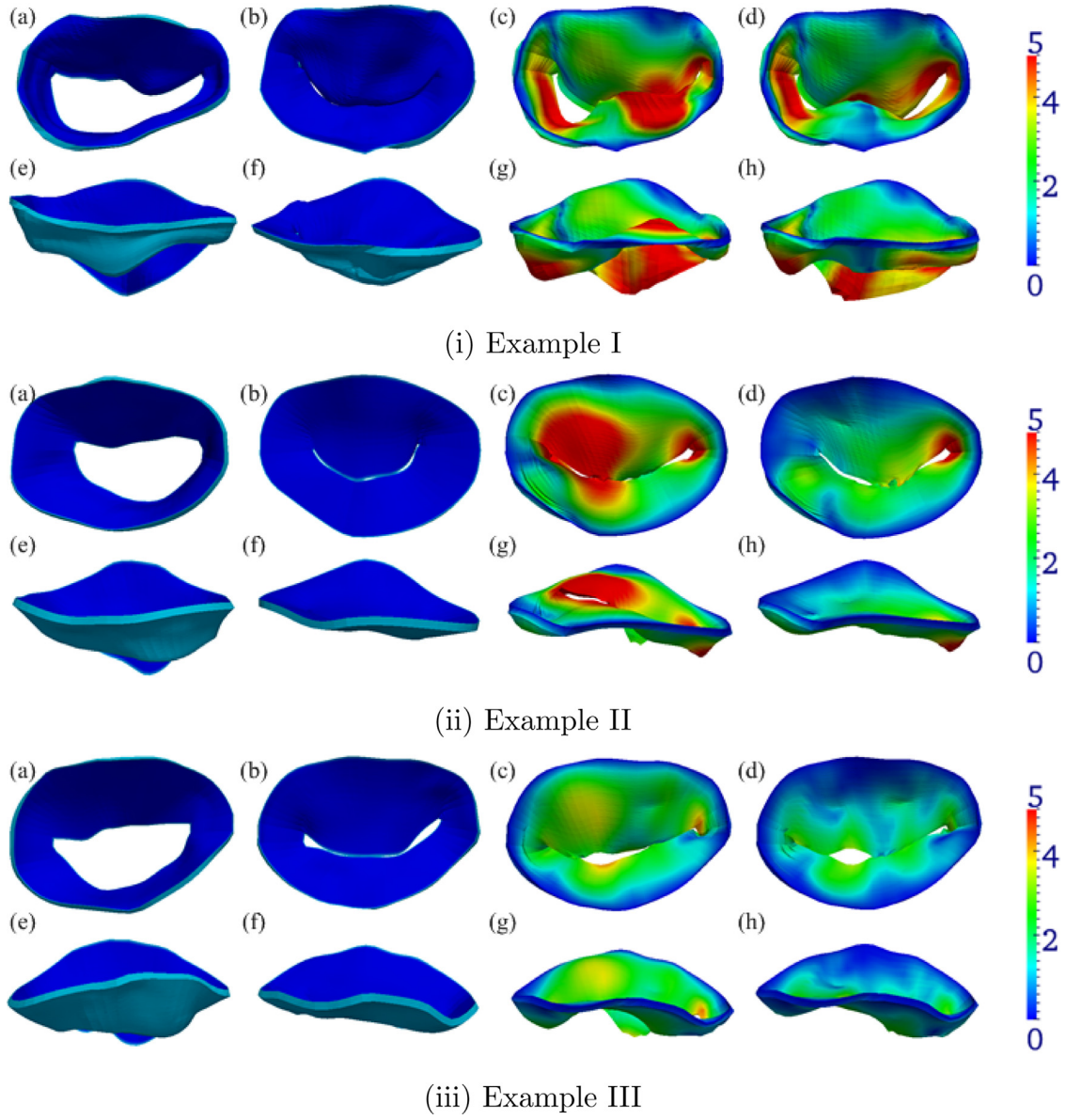

Fig. 4. Demonstration of chordae rest length optimization. Mitral leaflet extracted from the TEE images at the end diastole: (a)(e), at the early systole:(b)(f). Colored Euclidean distances between simulated and observed mitral valve closure with general : (c)(g), and adjusted: (d)(h) chordae rest length. Top view:(a)(b)(c)(d), Side view: (e)(f)(g)(h) of the mitral leaflet.(For interpretation of the references to colour in this figure legend, the reader is referred to the web version of this article.)

Table 4
Estimated material parameters.

	$E_f^{Anterior}$	$E_{f\perp}^{Anterior}$	$G^{Anterior}$	$E_f^{Posterior}$	$E_{f\perp}^{Posterior}$	$G^{Posterior}$
P1	5.49	2.07	1.84	0.55	0.49	0.18
P2	10.75	4.05	3.61	0.58	0.52	0.19
P3	5.47	2.06	1.84	1.27	1.15	0.43
P4	5.32	2.01	1.79	2.30	2.08	0.77
P5	4.74	1.79	1.59	2.66	2.41	0.89
P6	4.25	1.60	1.43	2.08	1.88	0.70
P7	5.32	2.01	1.79	1.76	1.59	0.59
P8	6.57	2.48	2.21	0.94	0.85	0.31
P9	4.34	1.64	1.46	2.30	2.08	0.77
P10_1	3.39	1.28	1.14	1.94	1.76	0.65
P10_2	4.99	1.88	1.68	1.18	1.06	0.39
P11	5.60	2.11	1.88	2.01	1.81	0.67
P12	3.71	1.40	1.24	3.58	3.23	1.20
P13	6.64	2.50	2.23	1.69	1.53	0.57
P14	5.00	1.88	1.83	1.79	1.62	0.60

P10_2), for which a patient-specific model is built based on the TEE images from two scans of the same patient, Young's modulus is smaller than the generic value for both the anterior and posterior leaflets. These results suggest that our algorithm can provide qualitative indications although it cannot ensure absolute quantitative accuracy.

The qualitative effects on the simulation results are demonstrated in two examples 5. In Fig. 5(i), material parameters optimization brings the average Euclidean distances from 2.59 ± 1.59 mm to 2.52 ± 1.33 mm. It also helps to close the regurgitation hole so that the simulation matches the observation with clinical relevance. In Fig. 5(ii), material parameters optimization greatly reduced the regurgitation hole and brings the average Euclidean distances from 2.88 ± 2.12 mm to 2.55 ± 1.76 mm. The estimation results indicate that the anterior leaflet is stiffer while the posterior leaflet is less stiff than the generic value. The simulation results are still not satisfactory for this patient because of the still large regurgitation hole. The unsatisfactory results partially orig-

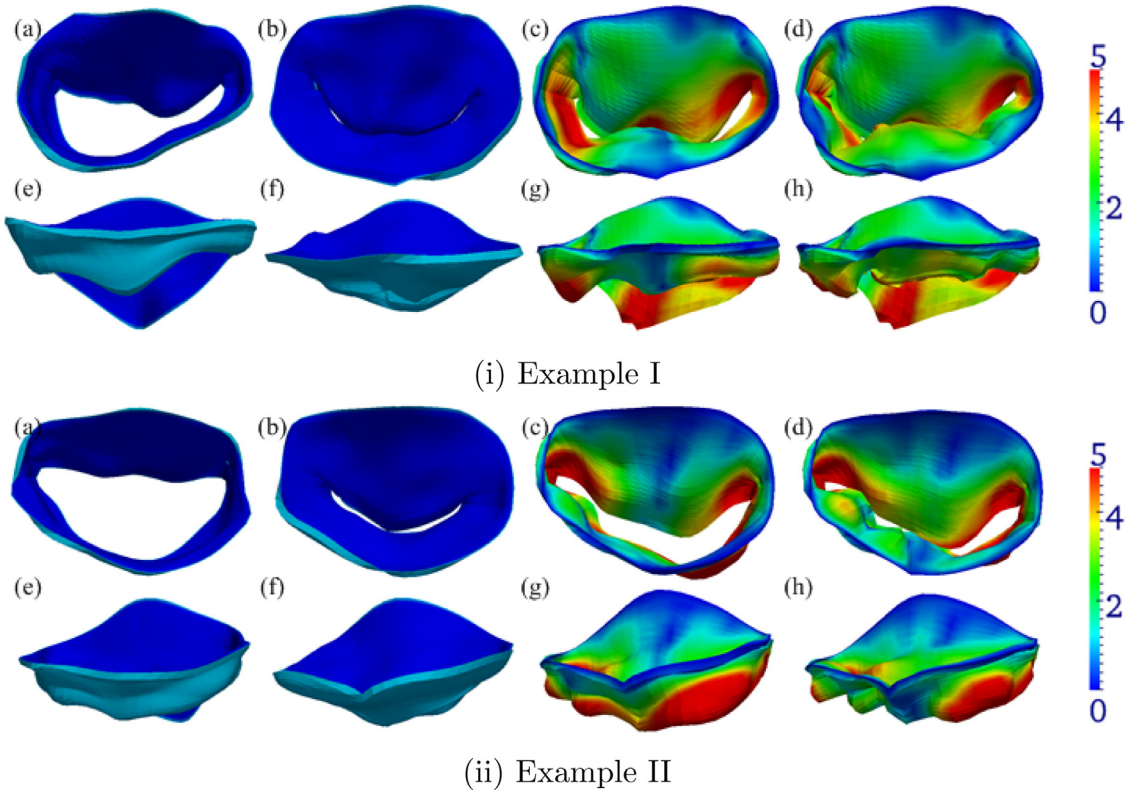

Fig. 5. Effect of material parameters on mitral valve closure simulation. Mitral leaflet extracted from the TEE images at the end diastole: (a)(e), at the early systole:(b)(f). Colored Euclidean distances between simulated and observed mitral valve closure with general : (c)(g), and estimated: (d)(h) material parameters. Top view:(a)–(d), Side view: (e)–(h) of the mitral leaflet.(For interpretation of the references to colour in this figure legend, the reader is referred to the web version of this article.)

inated from image analysis since both the anterior and posterior leaflet morphology is vastly different in the open and closed configuration.

4. Discussion and future direction

The personalization algorithm estimates the chordae rest length and material parameters by incorporating the image analysis module and the biomechanical module. Here we list several potential advancements in the future that could improve the performance of this parameter estimation.

Image analysis: The image analysis module reconstructs the morphology and dynamics of the mitral valve from in-vivo measurements. The open valve configuration is used in the biomechanical model as the initial geometry, and closed valve configuration as target in the cost function to match the simulation results. Inaccuracy in the image-derived geometry will have significant influence on the parameter estimation. The learning based image analysis algorithm used in the paper is tested on a large data set with error comparable the image resolution (Mansi et al., 2012). Advancement in imaging techniques can improve the visualization of the mitral valve apparatus to help differentiate the mitral valve tissues from the blood pool and noise. A comparison of algorithm performance using TEE and using other imaging modalities is of interest in order to investigate the capacity of each imaging modality to capture mitral valve geometry and dynamics information. Finally, inspection by the experts or clinicians of the results can help improve the accuracy and ensures the results are clinically relevant.

Cost function design: The problem is formulated in Eq. (8) to minimize the summed Euclidean distances between the simulated and estimated mitral valve closure. The cost function can be altered for more specific applications. Coaptation is another important evaluation standard for diagnosis and surgical outcomes.

When the mitral regurgitation is evaluated, it is important to allow the biomechanical model to simulate the regurgitation hole when the leaflets are observed to not fully close in the TEE images. In this case, the match at the edge of the leaflets may be more important than at the belly of the leaflets. It may be more appropriate to use a weighted sum of the distances. The biomechanical model used here aims to simulate mitral valve closure instead of the stress and strain analysis for the entire cardiac cycle. The simulated mitral valve at the closed configuration are compared to the ground truth instead of all the available frames between end diastole and early systole. In a different application or different model, the displacement at more time points can be used in the cost function.

Material parameters: Material parameters are assumed to be homogeneous within one leaflet and the relationship among the material parameters are fixed in this study. Since it is an initial attempt to estimate material parameters using noisy measurements from TEE images, the smallest number of estimates with strong constraint are chosen to ensure the physiological consistency of the parameters. As the problem is understood better, the constraints can be released by confining the relationship among Young's modulus along the fiber (E_f), Young's modulus across the fiber ($E_{f\perp}$) and shear modulus (G) and letting each parameter be independent. Besides, material parameters can be allowed to vary regionally within anterior and posterior leaflet to approximate the real tissue properties for normal and pathological mitral valve. The estimated material parameters have some qualitative indication but more quantitative evaluation is needed.

Other parameters: A fully personalized patient-specific model can be built with more measurement available and more detailed

assumptions on mitral valve morphology. Measured pressure for each patient instead of a generic profile can be used to improve the accuracy of the personalized forces. The thickness and density of the mitral leaflets for different patients at different locations may be assigned in-homogeneously to characterize the leaflets closer to reality. The number of chordae and the location of marginal and basal chordae are not identified from the TEE images limited by the image quality. Instead, fixed number of chordae with identical insertion points for all patients are used in the biomechanical model. The chordae distribution model is first proposed by Kunzelman and Cochran (1990) and has been proved to be efficient by other researchers for normal mitral valve simulations (Votta et al., 2008; 2013). In patients with pathological changes such as ruptured chordae, the distribution and properties of chordae may be vastly different. And the distribution of the chordae has a significant influence on the simulation results. Algorithms may be developed to evaluate if the distribution and properties of the chordae need to be adjusted before further optimization. Forces from heart pressure can be measured in-vivo in the left atrium and ventricle.

Population Study: This study utilized images from a sample population that was unselected with respect to the presence of mitral regurgitation. We plan to eventually conduct a systematic comparison of performance for both control subjects and patients with varying degrees of mitral regurgitation severity, but this initial effort was aimed at evaluating a new approach for noninvasively estimating in vivo material properties and chordae lengths. The ultimate goal would be to guide surgical decision making by predicting the effects of varying degrees of leaflet resection and/or artificial chord placement on mitral valve coaptation. In addition, though, this method could be used to acquire data aimed at building a statistical database for identifying normal and abnormal ranges for these parameters. From a modeling viewpoint, the initial contribution is to help build parametric models for this application area and provide a foundation for later development of more advanced subject-specific models.

5. Conclusions

The paper presented an streamlined framework to build a patient-specific biomechanical model of the mitral valve from TEE images with minimal user interaction. The framework combines image analysis and biomechanics to optimize chordae rest length and material parameters to ensure the biomechanical model simulated mitral valve closure matches the image based observations. Through the personalization, the mitral valve model is calibrated for individual patient. During the personalization, material parameters of human mitral valve are estimated from TEE images. Those efforts allow a user-friendly platform to build patient-specific models, thus bringing the quantitative computational modeling one step closer to clinical application.

The framework has three essential modules including an image analysis module, a biomechanical module and a model calibration module. During the model calibration process, chordae rest length and material parameters are optimized. The algorithm is tested on 15 sets of images for 14 patients yielding an average Euclidean distances of 1.86 ± 1.24 mm in simulating the mitral valve closure. The chordae rest length is optimized using a morphology guided search based algorithm. The chordae rest length adjustment reduced the simulation error to about 2 mm which is comparable to image resolution. Personalized material parameters further reduces the error and at times reduces the regurgitation hole. The estimated material parameters confirm that the anterior leaflet is stiffer than posterior leaflet (Imanaka et al., 2007), and that material parameters vary among patients.

Acknowledgments

The authors thank Siemens Corporation, Corporate Technology, for its funding to support the work, and Dr. Ben A. Lin for his insights during the discussions.

References

Barber, J.E., Kaspera, F.K., Ratliff, N.B., Cosgrove, D.M., Griffin, B.P., Vesely, I., 2001. Mechanical properties of myxomatous mitral valves. J. ThoracicCardiovasc. Surg. 122, 955–962.
Burlina, P., Sprouse, C., DeMenthon, D., Jorstad, A., Juang, R., Contijoch, F., Abraham, T., Yuh, D., McVeigh, E., 2010. Patient-specific modeling and analysis of the mitral valve using 3d-tee. In: Information Processing in Computer-Assisted Interventions, pp. 135–146.
Comas, O., Taylor, Z.A., Allard, J., Ourselin, S., Cotin, S., Passenger, J., 2008. Efficient nonlinear fem for soft tissue modelling and its gpu implementation within the open source framework sofa. In: Biomedical Simulation. Springer, pp. 28–39.
Einicke, G.A., White, L.B., 1999. Robust extended kalman filtering. IEEE Trans. Signal Process. 47, 2596–2599.
Einstein, D., Del Pin, F., Jiao, X., Kuprat, A., Carson, J., Kunzelman, K., Cochran, R., Guccione, J., Ratcliffe, M., 2010. Fluid-structure interactions of the mitral valve and left heart: comprehensive strategies, past, present and future. Int. J. Numer. Methods Biomed. Eng. 26, 348–380.
Fischler, M., Bolles, R., 1981. Random sample consensus: a paradigm for model fitting with applications to image analysis and automated cartography. Comm. ACM 24(6), 381–395.
Glower, D.D., 2012. Surgical approaches to mitral regurgitation. J. Am. College Cardiol. 60, 1315–1322.
Hammer, P., Chen, P., delNido, P., Howe, R., 2012. Computational model of aortic valve surgical repair using grafted pericardium. J. Biomech. 45(7), 1199–1204.
Hammer, P., Vasilyev, N., Perrin, D., Del Nido, P., Howe, R., 2008. Fast image-based model of mitral valve closure for surgical planning. In: Computational Biomechanics for Medicine (MICCAI Workshop), pp. 15–26.
Imanaka, K., Takamoto, S., Ohtsuka, T., Oka, T., Furuse, A., Omata, S., 2007. The stiffness of normal and abnormal mitral valves. Ann. Thoracic Cardiovasc. Surg. 13, 178.
Ionasec, R.I., 2010. Patient-specific modeling and quantification of the heart valves from multimodal cardiac images. Technical University Munich Ph.D. thesis.
Kanik, J., Mansi, T., Voigt, I., Sharma, P., Ionasec, R., Comaniciu, D., J., D., 2013a. Automatic personalization of the mitral valve biomechanical model based on 4d transesophageal echocardiography. Statistical atlases and computational models of the heart (MICCAI workshop).
Kanik, J., Mansi, T., Voigt, I., Sharma, P., Ionasec, R., Comaniciu, D., J., D., 2013b. Estimation of patient-specific material properties of the mitral valve using 4d transesophageal echocardiography. ISBI.
Krishnamurthy, G., Ennis, D., Itoh, A., Bothe, W., Swanson, J., Karlsson, M., Kuhl, E., Miller, D., Ingels Jr, N., 2008. Material properties of the ovine mitral valve anterior leaflet in vivo from inverse finite element analysis. Am. J. Physiol. Heart Circulatory Physiol. 295, 1141–1149.
Krishnamurthy, G., Itoh, A., Bothe, W., Swanson, J., Kuhl, E., Karlsson, M., Craig Miller, D., Ingels, N., 2009. Stress-strain behavior of mitral valve leaflets in the beating ovine heart. J. Biomech. 42, 1909–1916.
Kunzelman, K., Cochran, K., 1990. Mechanical properties of basal and marginal mitral valve chordae tendineae. ASAIO Trans. 36(3), 8–405.
Kunzelman, K., Einstein, D., Cochran, R., 2007. Fluid-structure interaction models of the mitral valve: function in normal and pathological states. Philos. Trans. Royal Soc. B 362, 1393.
Liu, H., Shi, P., 2007. State-space analysis of cardiac motion with biomechanical constrains. IEEE Trans. Image Process. 16(4), 901–917.
Liu, H., Shi, P., 2009. Maximum a posteriori strategy for the simultaneous motion and material property estimation of the heart. IEEE Trans. Biomed. Eng. 56(2), 378–389.
Mann, D.L., Zipes, D.P., Libby, P., Bonow, R.O., 2014. Braunwald's Heart Disease: A Textbook of Cardiovascular Medicine. Elsevier Health Sciences.
Mansi, T., Voigt, I., Georgescu, B., Zheng, X., Mengue, E., Hackl, M., Ionasec, R., Noack, T., Seeburger, J., Comaniciu, D., 2012. An integrated framework for finite-element modeling of mitral valve biomechanics from medical images: application to mitralclip intervention planning. Med. Image Anal. 16 (Oct(7)), 46–1330.
Marchesseau, S., Sermesant, M., Billet, F., Delingette, H., Ayache, N., 2015. Personalization of electromechanical models of the cardiac ventricular function by heterogeneous clinical data assimilation. Multi-Modality Cardiac Imaging 293–330.
May-Newman, K., Yin, F., 1995. Biaxial mechanical behavior of excised porcine mitral valve leaflets. Am. J. Physiol. - Heart Circ. Physiol. 269, 1319–1327.
Nishimura, R.A., Vahanian, A., Eleid, M.F., Mack, M.J., 2016. Mitral valve diseasecurrent management and future challenges. The Lancet 387, 1324–1334.
Pham, T., Sun, W., 2014. Material properties of aged human mitral valve leaflets. J. Biomed. Mater. Res. Part A 102, 2692–2703.
Powell, M., 1964. An efficient method for finding the minimum of a function of several variables without calculating derivatives. Comput. J. 7(2), 155–162.
Prot, V., Haaverstad, R., Skallerud, B., 2009. Finite element analysis of the mitral apparatus: annulus shape effect and chordal force distribution. Biomech. Model. Mechanobiol. 8, 43–55.

Prot, V., Skallerud, B., 2009. Nonlinear solid finite element analysis of mitral valves with heterogeneous leaflet layers. Comput. Mech. 43, 353–368.
Rausch, M.K., Famaey, N., Shultz, T.O., Bothe, W., Miller, D.C., Kuhl, E., 2013. Mechanics of the mitral valve. Biomech. model. mechanobiol. 12, 1053–1071.
Schievano, S., Kunzelman, K., Nicosia, M., Cochran, R., Einstein, D., Khambadkone, S., Bonhoeffer, P., 2009. Percutaneous mitral valve dilatation: single balloon versus double balloon. a finite element study. J. Heart Valve Dis. 18, 28–34.
Schievano, S., Migliavacca, F., Coats, S., Khambadkone, L., Carminati, M., Wilson, N., Deanfield, J., Bonhoeffer, P., Taylor, A., 2007. Percutaneous pulmonary valve implantation based on rapid prototyping of right ventricular outflow tract and pulmonary trunk from mr data. Radiology 242, 49–490.
Schneider, R., Perrin, D., Vasilyev, N., Marx, G., del Nido, P., Howe, R., 2012. Mitral annulus segmentation from four-dimensional ultrasound using a valve state predictor and constrained optical flow. Med. Image Anal. 16(2), 497–504.
Sprouse, C., Mukherjee, R., Burlina, P., 2013. Mitral valve closure prediction with 3d personalized anatomical models and anisotropic hyperelastic tissue assumptions. IEEE Trans. Biomed. Eng. 60(11), 47–3238.
Stephens, E.H., de Jonge, N., McNeill, M.P., Durst, C.A., Grande-Allen, K.J., 2009. Age-related changes in material behavior of porcine mitral and aortic valves and correlation to matrix composition. Tissue Eng. Part A 16, 867–878.
Stevanella, M., Krishnamurthy, G., Votta, E., Swanson, J., Redaelli, A., Ingels, N., 2011. Mitral leaflet modeling: importance of in vivo shape and material properties. J. Biomech. 44, 2229–2235.
Sun, W., Martin, C., Pham, T., 2014. Computational modeling of cardiac valve function and intervention. Annu. Rev. Biomed. Eng. 16, 53–76.
Tu, Z., 2005. Probabilistic boosting-tree: learning discriminative methods for classification, recognition, and clustering. In: Computer Vision, pp. 1589–1596.
Veronesi, F., Corsi, C., Sugeng, L., Mor-Avi, V., Caiani, E., Weinert, L., Lamberti, C., Lang, R., 2009. A study of functional anatomy of aortic-mitral valve coupling using 3d matrix transesophageal echocardiography. Circulation: Cardiovasc. Imaging 2, 24–31.
Votta, E., Caiani, E., Veronesi, F., Soncini, M., Montevecchi, F., Redaelli, A., 2008. Mitral valve finite-element modelling from ultrasound data: a pilot study for a new approach to understand mitral function and clinical scenarios. Philos. Trans. A Math. Phys. Eng. Sci. 366(1879), 34–3411.
Votta, E., Le, T., Stevanella, M., Fusini, L., Caiani, E., Redaelli, A., Sotiropoulos, F., 2013. Toward patient-specific simulations of cardiac valves: State-of-the-art and future directions. J. Biomech. 46(2), 28–217.
Wang, Q., Sun, W., 2013. Finite element modeling of mitral valve dynamic deformation using patient-specific multi-slices computed tomography scans. Ann. Biomed. Eng. 41(1), 53–142.
Watton, P., Luo, X., Yin, M., Bernacca, G., Wheatley, D., 2008. Effect of ventricle motion on the dynamic behaviour of chorded mitral valves. J. Fluids Struct. 24, 58–74.
Wong, K.C., Wang, L., Zhang, H., Liu, H., Shi, P., 2011. Physiological fusion of functional and structural images for cardiac deformation recovery. Med. Imaging IEEE Trans. 30, 990–1000.
Yang, L., Georgescu, B., Zheng, Y., Meer, P., Comaniciu, D., 2008. 3-d ultrasound tracking of the left ventricle using one-step forward prediction and data fusion of collaborative trackers. Computer Vision and Pattern Recognition.
Zheng, Y., Barbu, A., Georgescu, B., Scheuering, M., Comaniciu, D., 2008. Four-chamber heart modeling and automatic segmentation for 3-d cardiac ct volumes using marginal space learning and steerable features. IEEE Trans. Med. Imaging 27(11), 1668–1681.
Zhou, X., Yang, C., Yu, W., 2012. Automatic mitral leaflet tracking in echocardiography by outlier detection in the low-rank representation. In: Computer Vision and Pattern Recognition, pp. 972–979.